Adaptive Hierarchical Representation Alliance for Multimodal Learning

Anonymous ACL submission

Abstract

Multimodal models often align language, vision, and audio in a single final-layer latent space, implicitly assuming that task-relevant evidence emerges at the same semantic depth across modalities. Using layer-wise CKA analysis, we observe that this assumption leads to semantic granularity mismatch: textual cues usually require deeper contextual abstraction, whereas visual and acoustic cues often provide discriminative perceptual evidence in shallow or middle layers. This mismatch can flatten fine-grained modality-private cues and reduce reliability under noisy, imbalanced, or missing inputs. To address this, we proposed Adaptive Hierarchical Representation Alliance (AHRA), a hierarchical shared–private expert framework. AHRA factorizes each modality into shared and private streams across semantic levels, regularizes them with shared alignment and private decorrelation, routes shared information through a cross-modal expert, and enhances task-relevant private tokens with modality-specific experts guided by a sparsity-controlled soft-gating mechanism (foreground exam). A hierarchical co-fusion module then performs intra-level expert coordination and inter-level semantic selection. Experiments on six benchmarks across image-text classification, multimodal intent recognition, and trimodal sentiment analysis show that AHRA consistently improves over strong baselines and remains robust under noisy and missing-modality settings.

1 Introduction

Multimodal Learning (MML) integrates heterogeneous signals such as language, vision, and audio into unified representations for tasks including sentiment analysis, intent recognition, and multimodal classification (Meng et al., 2026c,d). The central challenge is modality heterogeneity: different signals vary in temporal scale, statistical distribution, and abstraction level (Fang et al., 2025; Li et al., 2026; Meng et al., 2026b). Existing methods mainly address this challenge through two directions. Representation disentanglement separates modality-invariant and modality-specific factors (Meng et al., 2026c,d; Hazarika et al., 2020; Yang et al., 2022; Wang et al., 2025; Yang et al., 2023a; Li et al., 2023), while dynamic or robust fusion calibrates modality contributions under noise, imbalance, or missing inputs (Zhang et al., 2024, 2023; Gao et al., 2024; Wu et al., 2025; Li et al., 2026; Yang et al., 2023b; Meng et al., 2026a). Although effective, most methods still perform alignment, calibration, and prediction in a single terminal latent space. This flat protocol implicitly assumes that task-relevant evidence from all modalities emerges at the same semantic depth.

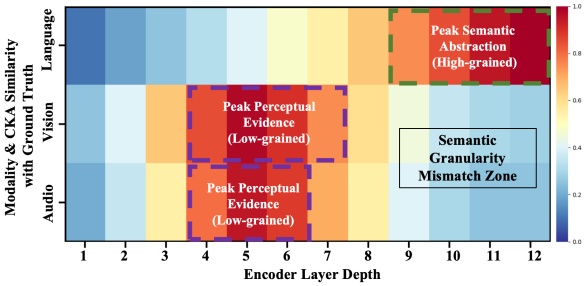

Figure 1: Layer-wise CKA similarity with labels. Text peaks in deep layers, while vision and audio peak in shallow or middle layers, revealing Semantic Granularity Mismatch (SGM) and motivating hierarchical fusion.

We argue that this assumption overlooks **Semantic Granularity Mismatch (SGM)**. Language is symbolic and compositional, so its discriminative semantics often require deep contextual abstraction. In contrast, visual and acoustic signals are perceptual: cues such as facial movements, objects, tone, or prosody may already be informative in shallow or middle layers. To examine this divergence, we conduct a layer-wise semantic analysis using Centered Kernel Alignment (CKA) (Kornblith et al., 2019) between hidden representations and task la-

bels:

$$\mathrm{CKA}(K, L) = \frac{\mathrm{HSIC}(K, L)}{\sqrt{\mathrm{HSIC}(K, K)\mathrm{HSIC}(L, L)}}, \tag{1}$$

where K and L denote kernel matrices constructed from layer-wise representations and labels, respectively, and HSIC denotes the Hilbert–Schmidt Independence Criterion. As shown in Fig. 1, text reaches its strongest label correlation in deep layers, whereas vision and audio peak earlier. Final-layer alignment can force low-granularity perceptual evidence into an overly abstract space, causing useful modality-private details to be diluted.

SGM leads to two practical failures. First, feature flattening suppresses fine-grained perceptual cues as background variation when they are projected into deep semantic spaces. Second, inference rigidity makes the model less able to rely on trustworthy unimodal evidence when modalities conflict, are corrupted, or are partially missing. These failures suggest that multimodal fusion should not only align modalities globally, but preserve and select evidence across different semantic levels.

To address this problem, we propose **Adaptive Hierarchical Representation Alliance (AHRA)**. As illustrated in Fig. 2, AHRA extracts multi-level features from each modality and factorizes them into shared and private streams at every semantic level. The shared streams capture cross-modal agreement, while the private streams retain modality-specific cues that may be lost under single-space fusion. This decomposition is regularized by shared alignment and private decorrelation, preventing the model from collapsing back into a single latent space. On top of these streams, an Adaptive Expert Alliance (AEA) applies a cross-modal expert to shared representations and modality-specific experts to private representations, with a sparsity-regularized foreground exam softly emphasizing task-relevant private tokens. A Hierarchical Multi-Expert Co-Fusion module (HMEC) then performs intra-level expert coordination and inter-level semantic selection to produce the final multimodal representation. More related works see Appendix A. Our contributions are as follow:

- We identify **Semantic Granularity Mismatch (SGM)** as a structural limitation of single-space multimodal fusion, and provide layer-wise CKA evidence showing that language, vision, and audio reach peak label correlation at different semantic depths.
- We propose **Adaptive Hierarchical Representation Alliance (AHRA)**, a hierarchical shared-private expert framework that preserves modality-private cues across multiple semantic levels while maintaining cross-modal agreement.
- We design **Adaptive Expert Alliance (AEA)** and **Hierarchical Multi-Expert Co-Fusion (HMEC)** to perform adaptive private-token enhancement, intra-level expert coordination, and inter-level semantic selection, leading to strong performance on six multimodal benchmarks across image–text classification, multimodal intent recognition, and trimodal sentiment analysis, including noisy and missing-modality settings.

2 Methodology

2.1 Model Overview

We consider supervised multimodal learning over a set of dataset-level modalities $\mathcal{M} \subseteq \{L, V, A\}$, where L, V, and A denote language, vision, and audio. For trimodal datasets, $\mathcal{M} = \{L, V, A\}$; for image–text datasets, $\mathcal{M} = \{L, V\}$. Let $(m_1, \ldots, m_{|\mathcal{M}|})$ be a fixed modality ordering and define

$$\mathcal{P} = \{(m_a, m_b) : 1 \leq a < b \leq |\mathcal{M}|\}. \tag{2}$$

Here $\mathcal{M}$ refers to dataset-level modalities; sample-level missing or imbalanced modalities are evaluated in the robustness experiments.

Adaptive Hierarchical Representation Alliance (AHRA) addresses semantic granularity mismatch by combining multi-level shared–private factorization with adaptive expert routing. At each semantic level, AHRA projects each modality into a shared stream and a private stream. The shared streams are regularized for cross-modal coordinate compatibility, while the private streams are regularized only through linear decorrelation rather than a hard independence constraint. An Adaptive Expert Alliance (AEA) routes shared streams to a cross-modal expert and foreground-weighted private streams to modality-specific experts. A Hierarchical Multi-Expert Co-Fusion module (HMEC) then performs intra-level expert coordination and inter-level semantic aggregation.

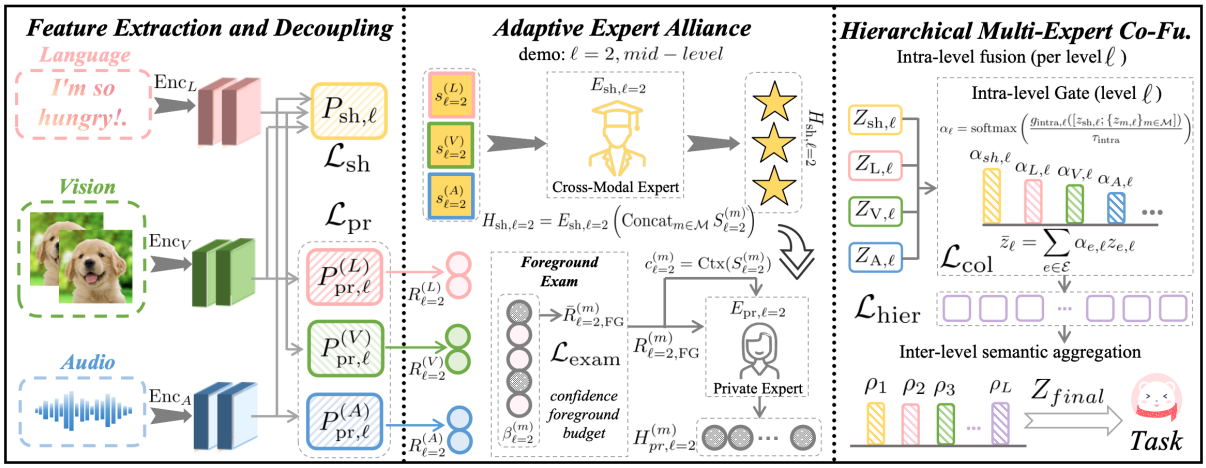

Figure 2: Overview of AHRA. The trimodal case is shown for illustration. For each modality $m \in \mathcal{M}$ and semantic level ℓ, AHRA factorizes encoder features into shared streams $S_\ell^{(m)}$ and private streams $R_\ell^{(m)}$, routes them through a shared-space cross-modal expert and foreground-controlled modality-specific experts, and obtains z_{final} via intra-level expert co-fusion and inter-level semantic aggregation.

2.2 Semantic Granularity Diagnostic

AHRA is motivated by semantic granularity mismatch: different modalities may reach their strongest task-dependent representations at different encoder depths. For diagnostic CKA, ℓ indexes evaluated encoder depths; for AHRA training, selected depths are grouped into L semantic levels, e.g., shallow, middle, and deep. For modality m, depth/level ℓ, and sample i, we define $h_{\ell,i}^{(m)} = \text{Pool}(H_{\ell,i}^{(m)})$, $D_{m,\ell} = \text{Dep}(\{h_{\ell,i}^{(m)}\}_{i=1}^n, \{y_i\}_{i=1}^n)$, $\ell_m^\star = \arg\max_\ell D_{m,\ell}$. In our diagnostic analysis, $\text{Dep}(\cdot,\cdot)$ is estimated by Centered Kernel Alignment (CKA) between representation and label kernels. The semantic granularity mismatch score is

$$\text{SGM} = \frac{1}{|\mathcal{P}|} \sum_{(m,m')\in\mathcal{P}} \left| \frac{\ell_m^*}{L_m} - \frac{\ell_{m'}^*}{L_{m'}} \right|. \quad (3)$$

The CKA analysis is used as an empirical diagnostic rather than a formal proof; it motivates retaining multiple semantic levels instead of relying only on final-layer fusion.

2.3 Multi-Level Shared–Private Factorization

Semantic levels and projections. For each modality $m \in \mathcal{M}$, a unimodal encoder extracts L semantic levels,

$$\{H_\ell^{(m)}\}_{\ell=1}^L = \text{Enc}_m(x^{(m)}), \quad H_\ell^{(m)} \in \mathbb{R}^{T_\ell^{(m)} \times d}. \quad (4)$$

If raw backbone widths differ, the corresponding width-matching adapter is absorbed into $\text{Enc}_m(\cdot)$, so all $H_\ell^{(m)}$ have the common width d. At level ℓ, AHRA applies a modality-agnostic shared projector and modality-specific private projectors:

$$S_\ell^{(m)} = H_\ell^{(m)} P_{\text{sh},\ell}, \quad R_\ell^{(m)} = H_\ell^{(m)} P_{\text{pr},\ell}^{(m)}, \quad (5)$$

where $P_{\text{sh},\ell} \in \mathbb{R}^{d\times d_{\text{sh}}}$ and $P_{\text{pr},\ell}^{(m)} \in \mathbb{R}^{d\times d_{\text{pr}}}$. The shared stream captures cross-modal common factors, while the private stream preserves modality-specific residual factors. These losses encourage separation but do not assume statistically identifiable disentanglement.

Shared alignment. For each sample, we mean-pool the shared tokens and standardize each coordinate over the mini-batch:

$$s_{\ell,i}^{(m)} = \frac{1}{T_\ell^{(m)}} \sum_{t=1}^{T_\ell^{(m)}} S_{\ell,i}^{(m)}[t,:], \; \hat{s}_{\ell,i,j}^{(m)} = \frac{s_{\ell,i,j}^{(m)} - \mu_{\ell,j}^{(m)}}{\sigma_{\ell,j}^{(m)} + \epsilon}. \quad (6)$$

This is dimension-wise standardization and does not whiten the full covariance matrix. The empirical cross-modal correlation matrix is

$$C_{\text{sh},\ell}^{(m,m')} = \frac{1}{B} \sum_{i=1}^{B} \hat{s}_{\ell,i}^{(m)} \hat{s}_{\ell,i}^{(m')\top} \in \mathbb{R}^{d_{\text{sh}}\times d_{\text{sh}}}. \quad (7)$$

AHRA uses the identity-shaped correlation loss

$$\mathcal{L}_{\text{sh}} = \frac{1}{L|\mathcal{P}|} \sum_{\ell=1}^{L} \sum_{(m,m')\in\mathcal{P}} \left\| C_{\text{sh},\ell}^{(m,m')} - I \right\|_F^2. \quad (8)$$

The diagonal terms encourage coordinate-wise cross-modal agreement, and the off-diagonal

terms reduce cross-coordinate redundancy. Since $C_{\mathrm{sh},\ell}^{(m,m')}$ is estimated from finite mini-batches, this loss is used as a stochastic correlation-shaping regularizer rather than an exactly attainable hard constraint in every batch.

Private linear decorrelation. Applying the same pooling and standardization to private streams gives $\hat{r}_{\ell,i}^{(m)}$. The private regularizer contains intra-modality shared–private decorrelation and cross-modality private–private decorrelation:

$$\mathcal{L}_{\mathrm{pr}}^{\mathrm{intra}} = \frac{1}{L|\mathcal{M}|} \sum_{\ell=1}^{L} \sum_{m\in\mathcal{M}} \left\| \frac{1}{B} \sum_{i=1}^{B} \hat{s}_{\ell,i}^{(m)} \hat{r}_{\ell,i}^{(m)\top} \right\|_F^2, \quad (9)$$

$$\mathcal{L}_{\mathrm{pr}}^{\mathrm{cross}} = \frac{1}{L|\mathcal{P}|} \sum_{\ell=1}^{L} \sum_{(m,m')\in\mathcal{P}} \left\| \frac{1}{B} \sum_{i=1}^{B} \hat{r}_{\ell,i}^{(m)} \hat{r}_{\ell,i}^{(m')\top} \right\|_F^2. \quad (10)$$

Then

$$\mathcal{L}_{\mathrm{dec}} = \lambda_{\mathrm{sh}} \mathcal{L}_{\mathrm{sh}} + \lambda_{\mathrm{pr}} \left(\mathcal{L}_{\mathrm{pr}}^{\mathrm{intra}} + \mathcal{L}_{\mathrm{pr}}^{\mathrm{cross}} \right). \quad (11)$$

The private loss penalizes linear cross-correlation and reduces duplicated linear factors, but it is not claimed to guarantee full statistical independence. Private streams remain task-grounded through the downstream task loss and private experts.

2.4 Adaptive Expert Alliance

AEA separates cross-modal reasoning from modality-private enhancement. For each semantic level, it constructs one shared-space cross-modal expert and one private expert for each available modality.

Shared-space cross-modal expert. At level ℓ, shared tokens are concatenated and passed to a cross-modal expert:

$$H_{\mathrm{sh},\ell} = E_{\mathrm{sh},\ell} \left(\mathrm{Concat}_{m\in\mathcal{M}}\, S_\ell^{(m)} \right). \quad (12)$$

The expert is implemented as a lightweight attention block, so cross-modal interactions are input-dependent but restricted to the shared subspace.

Private-space foreground exam. For modality m at level ℓ, each private token receives a soft foreground score:

$$\beta_{\ell,i,t}^{(m)} = \sigma \left((w_\ell^{(m)})^\top r_{\ell,i,t}^{(m)} + b_\ell^{(m)} \right). \quad (13)$$

$$R_{\ell,\mathrm{FG}}^{(m)} = \left\{ \beta_{\ell,i,t}^{(m)} r_{\ell,i,t}^{(m)} \right\}_{t=1}^{T_\ell^{(m)}}. \quad (14)$$

A modality-specific expert enhances the foreground-weighted private stream under same-level shared context:

$$c_\ell^{(m)} = \mathrm{Ctx}(S_\ell^{(m)}), H_{\mathrm{pr},\ell}^{(m)} = E_{\mathrm{pr},\ell}^{(m)} \left(R_{\ell,\mathrm{FG}}^{(m)};\, c_\ell^{(m)} \right). \quad (15)$$

Here $\mathrm{Ctx}(\cdot)$ denotes the shared-context representation used by the implementation, and the semicolon indicates conditioning rather than a separate prediction branch. This keeps the private expert anchored in foreground-weighted private tokens while allowing shared context to calibrate private-token enhancement.

Foreground budget and confidence. To avoid notation conflict with inter-level weights, we denote the target foreground ratio by $\pi_{m,\ell}$. The average foreground rate is $\bar{\beta}_{m,\ell} = \mathbb{E}_{i,t}[\beta_{\ell,i,t}^{(m)}]$. The exam regularizer is

$$\mathcal{L}_{\mathrm{exam}} = \sum_{\ell=1}^{L} \sum_{m\in\mathcal{M}} \Big[\lambda_{\mathrm{rate}} (\bar{\beta}_{m,\ell} - \pi_{m,\ell})^2 + \lambda_{\mathrm{conf}} \mathbb{E}_{i,t} \big[\beta_{\ell,i,t}^{(m)} (1 - \beta_{\ell,i,t}^{(m)}) \big] \Big] \quad (16)$$

The rate term controls the soft token budget, and the confidence term discourages ambiguous gates near 0.5.

2.5 Hierarchical Multi-Expert Co-Fusion

HMEC factorizes routing into intra-level expert coordination and inter-level semantic aggregation. For compactness, we omit the sample index in the following routing equations; all expert and level weights are computed per sample.

Intra-level expert co-fusion. At level ℓ, the shared expert output and private expert outputs are pooled into descriptors $z_{\mathrm{sh},\ell}$ and $\{z_{m,\ell}\}_{m\in\mathcal{M}}$. Let $\mathcal{E} = \{\mathrm{sh}\} \cup \mathcal{M}$ denote the expert index set. The intra-level gate is

$$\alpha_\ell = \mathrm{softmax} \left(\frac{g_{\mathrm{intra},\ell}([z_{\mathrm{sh},\ell}; \{z_{m,\ell}\}_{m\in\mathcal{M}}])}{\tau_{\mathrm{intra}}} \right) \quad (17)$$

and $\bar{z}_\ell = \sum_{e\in\mathcal{E}} \alpha_{e,\ell} z_{e,\ell}$.

Inter-level semantic aggregation. The inter-level gate assigns semantic-level weights and produces the final representation:

$$\rho = \mathrm{softmax} \left(\frac{\psi_{\mathrm{inter}}([\bar{z}_1; \ldots; \bar{z}_L])}{\tau_{\mathrm{inter}}} \right) \quad (18)$$

and $z_{\text{final}} = \sum_{\ell=1}^{L} \rho_\ell \bar{z}_\ell$. Equivalently, HMEC factorizes the joint routing distribution as

$$p(e, \ell \mid x) = p(\ell \mid x) p(e \mid \ell, x),$$

separating expert selection from semantic-level aggregation.

Gate regularization. For intra-level gates, AHRA discourages systematic under-use of private experts:

$$\mathcal{L}_{\text{col}} = \lambda_{\text{fair}} \sum_{m \in \mathcal{M}} [\max(0, \eta_m - \mathbb{E}_{x,\ell}[\alpha_{m,\ell}])]^2 \tag{19}$$

Here η_m is a small positive lower-usage prior for private experts, not a full target distribution over all experts. The actual expert distribution is mainly determined by the task loss and sample-dependent gates.

For inter-level aggregation, AHRA uses the entropy-form regularizer

$$\mathcal{L}_{\text{hier}} = \lambda_{\text{hier}} \sum_{\ell=1}^{L} \rho_\ell \log(\rho_\ell + \epsilon). \tag{20}$$

Since $\sum_\ell \rho_\ell \log \rho_\ell = -H(\rho)$, minimizing $\mathcal{L}_{\text{hier}}$ with $\lambda_{\text{hier}} > 0$ mildly encourages distributed level usage and prevents premature collapse to a single level. It is a level-diversity stabilizer rather than a sparsity or concentration penalty.

2.6 Learning Objective

The final prediction is produced by a task-specific head $\hat{y} = f_{\text{task}}(z_{\text{final}})$. For classification, f_{task} is a two-layer MLP with dropout 0.1 and outputs logits, for MOSI/MOSEI regression, it outputs a scalar sentiment score. Raw logits are passed directly to BCEWithLogits or CE without an explicit sigmoid or softmax. The overall objective is:

$$\mathcal{L}_{\text{total}} = \mathcal{L}_{\text{task}} + \mathcal{L}_{\text{dec}} + \mathcal{L}_{\text{exam}} + \mathcal{L}_{\text{col}} + \mathcal{L}_{\text{hier}}. \tag{21}$$

The task loss is dataset-dependent:

$$\mathcal{L}_{\text{task}} = \begin{cases} \text{BCEWithLogits}(\hat{y}, y), \\ \text{CE}(\hat{y}, y), \\ \text{MSE}(\hat{y}, y). \end{cases} \tag{22}$$

for multi-label classification, single-label classification and sentiment regression. MM-IMDB uses BCEWithLogits for multi-label genre prediction. Food101, MVSA-Single, and MIntRec use CE, MOSI/MOSEI use MSE and are evaluated by MAE, Acc-7, and F1. All auxiliary losses are computed only over available modalities and valid modality pairs. See Appendix B for details.

Table 1: Performance comparison across three benchmarks (%). Report the average result (%) from 5 random seeds.

Methods	MM-IMDB		Food101		MVSA-Single	
	F1-mic	F1-mac	Acc	F1	Acc	F1
ConCat	49.76	52.58	88.20	88.19	65.89	65.43
LateFu	59.56	58.91	90.69	90.77	76.88	75.72
GMU	63.00	54.10	90.38	84.86	75.31	70.82
MGMU	66.30	61.60	91.05	90.33	76.03	74.99
MMBT	66.80	61.80	94.10	91.28	78.50	-
TMC	66.80	61.80	89.86	89.80	76.06	74.55
QMF	-	-	92.92	92.93	78.90	77.18
EAU	-	-	93.20	93.18	79.15	78.36
MLA	-	-	93.33	-	**79.84**	-
BPMulT	68.90	58.70	-	-	-	-
ARL	-	-	93.55	93.55	-	-
AHRA	**69.18**	**63.24**	**95.06**	**94.21**	**79.84**	**78.59**

Table 2: Performance Comparison on the MIntRec (%).

Methods	Acc.	F1	Pre.	Rec.
Concat	68.54	66.22	66.90	66.10
LateFusion	69.21	67.01	67.88	67.13
MAG-BERT	70.34	68.19	68.31	69.36
MuLT	72.58	69.36	70.73	69.47
MISA	72.36	70.57	71.24	70.41
DLF	72.42	70.68	71.26	70.39
TSDA	72.61	71.43	72.13	70.74
EMOE	72.58	71.47	72.08	70.86
AHRA	**73.02**	**72.16**	**72.97**	**71.36**

3 Experiments

3.1 Datasets and Implementation Details

We evaluate AHRA on six multimodal benchmarks, including four classification datasets (MM-IMDB (Ma et al., 2022), Food101 (Bossard et al., 2014), MVSA-Single (Niu et al., 2016), and MIntRec (Zhang et al., 2022)) and two trimodal sentiment analysis datasets (CMU-MOSI (Zadeh et al., 2016) and CMU-MOSEI (Zadeh et al., 2018)). For the classification datasets, we follow EAU (Gao et al., 2024) and report accuracy, micro-F1, and macro-F1. For MOSI and MOSEI, we follow EMOE (Fang et al., 2025) and report MAE, Acc-7, and F1. AHRA is implemented in PyTorch and trained on four NVIDIA A100 GPUs. We use a unified training configuration across datasets unless otherwise specified, with early stopping based on validation F1. Detailed dataset and implementation information is provided in Appendices C and D. We evaluate AHRA against representative baselines, detailed descriptions and citations are deferred to Appendix E.

Table 3: Performance Comparison on MOSI and MOSEI. ↓ indicate that lower value is better.

Methods	CMU-MOSI			CMU-MOSEI		
	MAE↓	Acc7(%)	F1(%)	MAE↓	Acc7(%)	F1(%)
TFN	0.947	31.9	77.95	0.572	51.6	78.96
MulT	0.846	40.05	81.66	0.673	48.37	80.86
PMR	0.895	40.60	79.83	0.645	48.88	81.56
MISA	0.788	41.27	82.43	0.594	51.43	82.13
FDMER	0.760	42.88	83.22	0.571	53.21	83.35
DMD	0.744	43.88	83.55	0.561	54.18	83.88
MCIS	0.756	43.58	83.85	0.557	53.85	84.34
CGGM	0.747	43.21	84.13	0.551	53.47	84.14
ConFEDE	-	42.33	85.53	-	54.51	85.84
DiCMoR	-	45.3	85.6	-	53.4	85.1
DEVA	-	46.33	84.45	-	52.28	83.75
I2RL	-	47.06	86.21	-	54.72	86.46
DLF	0.731	47.08	85.04	0.536	53.9	85.27
EMOE	0.710	47.7	85.4	0.536	54.1	85.3
AHRA	**0.702**	**48.77**	**86.36**	**0.522**	**55.65**	**86.66**

Table 4: F1-macro (%) on MM-IMDB with varying image/text ratios. The baselines used are all from PEFT.

Training Image/Text	Testing Image/Text	ViLT	Lee	Uni.	PEFT	AHRA
100%/30%	100%/30%	32.78	37.72	39.47	43.21	**54.28**
	30%/100%	26.58	21.68	42.12	54.67	**62.93**
	65%/65%	30.55	30.80	40.99	49.09	**58.15**
	Average.	29.97	30.07	40.86	48.99	**58.45**
30%/100%	100%/30%	30.25	24.93	29.85	43.07	**50.67**
	30%/100%	37.97	47.10	54.37	56.03	**63.37**
	65%/65%	34.45	36.76	37.61	49.81	**53.96**
	Average.	34.22	36.26	40.61	49.64	**56.00**
65%/65%	100%/30%	35.80	39.04	40.60	42.46	**55.09**
	30%/100%	36.65	42.68	53.19	55.26	**63.43**
	65%/65%	36.66	41.33	47.34	49.24	**58.65**
	Average.	36.37	41.02	47.04	48.99	**59.06**

Table 5: Accuracy (%) of different methods on MVSA-Single under various noise levels.

Methods	Clean	Salt–Pepper		Gaussian	
	ϵ=0	ϵ=5	ϵ=10	ϵ=5	ϵ=10
Concat	65.59	58.69	51.16	50.70	46.12
Late Fusion	76.88	67.88	55.43	63.46	55.16
MMBT	78.50	74.07	51.26	71.99	55.34
TMC	74.87	68.02	56.62	66.72	60.35
QMF	78.07	73.90	60.41	73.85	61.28
EAU	79.15	74.81	61.40	73.89	62.04
AHRA	**79.84**	**76.43**	**62.20**	**73.98**	**63.37**

3.2 Comparison with the State-of-the-Art

We report the mean over five random seeds, with standard deviations provided in Appendix F.

We first compare AHRA with existing methods on the four classification benchmarks. As shown in Table 1 and Table 2, AHRA consistently matches or surpasses the strongest baselines. Specifically, on Food101, AHRA improves accuracy from 94.10 (MMBT (Kiela et al., 2020)) and 93.33 (MLA (Zhang et al., 2024)) to 95.06, and F1 from 93.18 (EAU (Gao et al., 2024)) to 94.21. On MIntRec, AHRA reaches 73.02 accuracy and 72.16 F1, outperforming the strongest reported baselines of 72.61 accuracy (TSDA (Meng et al., 2026d)) and 71.47 F1 (EMOE (Fang et al., 2025)). These results indicate that explicitly preserving modality-private information and routing it through private experts is beneficial for both image–text classification and trimodal intent recognition.

On the trimodal sentiment benchmarks CMU-MOSI and CMU-MOSEI, AHRA also achieves competitive or superior performance compared with recent multimodal models, as summarized in Table 3. On MOSI, AHRA reduces MAE compared with EMOE (Fang et al., 2025). On MOSEI, AHRA obtains the lowest MAE and the highest Acc-7 among the compared methods, while its F1 remains competitive with the strongest baseline. These results suggest that AHRA produces more informative multimodal representations for fine-grained sentiment prediction.

In summary, AHRA improves over prior methods on heterogeneous benchmarks by jointly factorizing features into shared and private streams and by using an adaptive expert hierarchy to select informative private tokens and semantic levels, thereby mitigating the dilution of modality specific cues inherent in single space fusion.

3.3 Robustness Analysis

We further evaluate AHRA under missing, imbalanced, and noisy modality conditions. On MM-IMDB, AHRA achieves the highest F1-macro across all image/text train–test availability ratios, including strongly mismatched distributions (Table 4), showing its ability to adapt modality reliance when one stream is undersampled or partially absent. On MVSA-Single, AHRA also obtains the best accuracy under both salt-and-pepper and Gaussian visual noise, with the smallest degradation as corruption increases (Table 5). These results indicate that shared–private separation, foreground-controlled private experts, and hierarchical co-fusion allow AHRA to suppress unreliable evidence and reallocate trust across modalities and semantic levels.

Table 6: Ablation Studies of the AHRA.

Setting	CMU-MOSI		Food101	
	MAE ↓	Acc-7(%)	Acc(%)	F1(%)
AHRA (Ours)	**0.702**	**48.77**	**95.06**	**94.21**
Importance of AHRA Components				
w/o AEA	0.724	47.10	94.02	93.30
w/o HMEC	0.716	47.65	94.35	93.65
Importance of Modality				
w/o Linguistic	0.864	38.10	93.85	93.02
w/o Acoustic	0.728	46.80	-	-
w/o Visual	0.735	45.50	88.90	88.75
Importance of Regularization				
w/o $\mathcal{L}_{\text{dec}}$	0.725	46.90	94.10	93.45
w/o $\mathcal{L}_{\text{exam}}$	0.716	47.40	94.32	93.70
w/o $\mathcal{L}_{\text{col}}$	0.708	48.15	94.72	93.98
w/o $\mathcal{L}_{\text{hier}}$	0.710	48.05	94.60	93.90

Table 7: Ablation on Fusion Mechanisms

Setting	CMU-MOSI		Food101	
	MAE ↓	Corr ↑	Acc(%)	F1(%)
AHRA (Ours)	**0.702**	**0.806**	**95.06**	**94.21**
Different Fusion Mechanisms				
Addition	0.746	0.762	94.05	93.28
Multiplication	0.741	0.771	94.25	93.50
CMAF	0.729	0.785	94.55	93.82

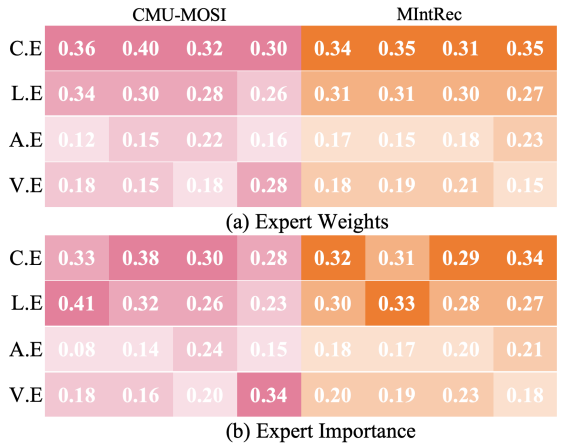

Figure 3: Visualization of learned expert weights and importance for AHRA. CE and LE dominate with selective AE/VE activation on MOSI, while all experts contribute more evenly on MIntRec, showing that expert allocation adapts to both data and task.

3.4 Ablation Studies

We conduct ablation studies on MOSI and Food101 to examine the contribution of each component in AHRA, with results reported in Table 6 and Table 7.

Effect of architectural components. Removing AEA consistently degrades performance on both datasets, showing that adaptive routing of private tokens through modality-specific experts is more effective than uniform private-feature processing. Removing HMEC also leads to performance drops, indicating that level-aware expert coordination is beneficial for jointly exploiting shared and private streams. These results confirm that AHRA preserves modality-private cues through the coupling of adaptive expert routing and hierarchical co-fusion.

Effect of modalities. Dropping any modality weakens performance, while the full multimodal setting achieves the best results. On MOSI, removing language causes the largest degradation, consistent with its dominant role in sentiment prediction, whereas audio and vision provide complementary private cues. On Food101, removing vision leads to the most severe drop, reflecting the visually dominant nature of fine-grained food recognition. This demonstrates that AHRA can exploit dominant modalities while still benefiting from complementary modality-specific information.

Effect of fusion mechanisms. Replacing HMEC with additive fusion, multiplicative fusion, or CMAF (Yang et al., 2022) consistently underperforms the full model. This suggests that hierarchical expert-level fusion is more suitable than fixed operators or single-stage attention for determining which experts and semantic levels should contribute to prediction.

Effect of regularization. Removing $\mathcal{L}_{\text{dec}}$ causes the most evident degradation, verifying the importance of aligning shared streams while decorrelating private streams to avoid collapse into a single latent space. Removing $\mathcal{L}_{\text{exam}}$ also hurts performance, indicating that sparse and confident foreground selection helps private experts focus on informative tokens. In contrast, dropping $\mathcal{L}_{\text{col}}$ or $\mathcal{L}_{\text{hier}}$ yields mild but consistent declines, suggesting that they mainly stabilize expert usage and level utilization rather than define the core representational capacity.

3.5 Visualization of Expert Weights and Importance.

To understand how AHRA allocates its experts, we visualize expert weights and expert importance on MOSI and MIntRec (Fig. 3). The expert weights are the fusion coefficients produced by HMEC for the cross-modal expert (CE) and the modality-specific experts (LE, AE, VE), while the expert importance reflects their estimated contributions to the final prediction. On MOSI, CE and LE gen-

Table 8: Effect of the foreground exam budget on CMU-MOSI and Food101. "FG ratio" denotes the achieved average foreground rate under the target budget π.

Setting	FG ratio (avg.)	CMU-MOSI		Food101	
		MAE ↓	Acc-7 (%)	Acc (%)	F1 (%)
No exam	100	0.716	47.40	94.32	93.70
$\pi = 0.15$	17	0.708	48.20	94.72	93.98
$\pi = 0.30$	**31**	**0.702**	**48.77**	**95.06**	**94.21**
$\pi = 0.45$	44	0.707	48.10	94.90	94.00
$\pi = 0.70$	69	0.712	47.80	94.65	93.85

Figure 4: Visualization of selected test cases from the MVSA-Single dataset. Our method consistently shows better robustness against noise in the three cases.

erally receive the largest weights and importance, whereas AE and VE are selectively amplified when prosodic or facial cues are salient. On MIntRec, the four experts are used in a more balanced manner, matching the setting where language, audio, and vision are all informative for intent recognition. Across both datasets, higher weights tend to coincide with higher importance, and different samples display distinct expert usage patterns. This indicates that AHRA exploits its expert bank in a data-dependent and task-aware way, rather than collapsing to a single dominant branch.

3.6 Analysis of the Foreground Exam Mechanism.

To clarify the role of the foreground exam, we vary a global foreground ratio $\pi \in \{0.15, 0.30, 0.45, 0.70\}$ in the exam loss while keeping all other components of AHRA fixed, and measure both the average fraction of private tokens emphasized by the soft foreground gate and performance on CMU-MOSI and Food101. We also include a variant without the exam, where all private tokens always enter the experts. As summarized in Table 8, the foreground budget controls the trade-off between selectivity and coverage: a very small budget ($\pi = 0.15$) activates too few private tokens and weakens modality-specific contributions, while a moderate budget ($\pi = 0.30$) yields the best results by filtering most background noise while retaining informative private tokens. Larger budgets ($\pi = 0.45$ and $\pi = 0.70$) gradually approach the no-exam variant, where many redundant or noisy private tokens are routed into the experts and performance declines. These results show that a moderate, sample-dependent foreground budget is crucial for selecting a compact yet informative subset of private tokens without either underusing private branches or overwhelming them with noise.

3.7 Qualitative Analysis

To examine the robustness of AHRA under noisy multimodal inputs, we visualize representative test cases with different noise levels in Fig. 4. Compared with the baseline method QMF (Zhang et al., 2023), which is more sensitive to input perturbations and tends to produce incorrect predictions, AHRA maintains more stable and accurate sentiment predictions. This qualitative comparison indicates that the proposed AEA and HMEC modules help suppress modality-specific noise and preserve reliable cross-modal evidence, thereby improving prediction stability under noisy conditions. More qualitative results are provided in Appendix G.

Complementary Analysis in the appendix further support AHRA: t-SNE visualization shows more compact and class-separable embeddings (Appendix H), sensitivity studies verify robustness to regularization coefficients (Appendix I), and efficiency results confirm that AHRA achieves strong performance with controlled computational cost (Appendix J).

4 Conclusion

In this paper, we proposed the Adaptive Hierarchical Representation Alliance (AHRA) to mitigate the dilution of modality-private information in single-space multimodal fusion. AHRA factorizes each modality into shared and private streams across multiple semantic levels and couples an Adaptive Expert Alliance, a foreground exam, and a Hierarchical Multi-Expert Co-Fusion module to selectively enhance private cues while coordinating cross-modal evidence. Experiments on image–text classification, multimodal intent recognition, and trimodal sentiment analysis under noisy and missing modality conditions show that AHRA consistently outperforms strong baselines and ablations, confirming its effectiveness and robustness for multimodal recognition.

Limitations

AHRA is evaluated on bimodal and trimodal benchmarks. Extending the framework to settings with many heterogeneous modalities, such as infrared, radar, depth, or physiological signals, may require additional modality selection or routing mechanisms to control computational cost and avoid expert over-fragmentation. In addition, AHRA does not explicitly address privacy risks, demographic bias, or dataset bias in multimodal data. These issues require further study before deployment in sensitive real-world applications.

Our SGM analysis relies on CKA between layer representations and task-label kernels. CKA provides a useful diagnostic of representation-label similarity, but it does not establish causal evidence about which layer should be used for fusion and may miss nonlinear label dependencies not captured by the chosen kernels. Future work can combine CKA with probing classifiers or causal intervention analyses.

Ethics Statement

This work studies multimodal representation learning on established academic benchmarks and does not introduce, collect, or release any new dataset. AHRA is evaluated on standard image–text classification, multimodal intent recognition, and trimodal sentiment analysis datasets, and all experiments are conducted for research purposes under their original benchmark settings. Since several benchmarks involve human-centered multimodal signals such as language, images, audio, or video, they may inherit annotation noise, demographic imbalance, privacy sensitivity, or social bias from the original data sources. Our method does not explicitly remove such dataset-level risks.

AHRA aims to improve robustness by preserving shared and modality-private evidence across semantic levels and by reducing reliance on unreliable or corrupted modalities. However, robustness to noisy or missing modalities should not be interpreted as a guarantee of fairness, privacy protection, or deployment safety. In particular, sentiment and intent recognition models may be misused for intrusive profiling, surveillance, or consequential decision-making if applied without appropriate consent and oversight. Therefore, AHRA should be regarded as a research framework and should not be directly deployed in sensitive real-world applications without dataset-specific bias audits, privacy assessment, human supervision, and compliance with the usage policies of the corresponding data sources.

References

John Arevalo, Thamar Solorio, Manuel Montes-y Gómez, and Fabio A González. 2017. Gated multimodal units for information fusion. *arXiv preprint arXiv:1702.01992*.

Lukas Bossard, Matthieu Guillaumin, and Luc Van Gool. 2014. Food-101 – mining discriminative components with random forests. In *European Conference on Computer Vision (ECCV)*, pages 446–461.

Yiyang Fang, Wenke Huang, Guancheng Wan, Kehua Su, and Mang Ye. 2025. Emoe: Modality-specific enhanced dynamic emotion experts. In *Proceedings of the Computer Vision and Pattern Recognition Conference*, pages 14314–14324.

Zixian Gao, Xun Jiang, Xing Xu, Fumin Shen, Yujie Li, and Heng Tao Shen. 2024. Embracing unimodal aleatoric uncertainty for robust multimodal fusion. In *Proceedings of the IEEE/CVF Conference on Computer Vision and Pattern Recognition (CVPR)*.

Zirun Guo, Tao Jin, Jingyuan Chen, and Zhou Zhao. 2024. Classifier-guided gradient modulation for enhanced multimodal learning. *Advances in Neural Information Processing Systems*, 37:133328–133344.

Zongbo Han, Changqing Zhang, Huazhu Fu, and Joey Tianyi Zhou. 2023. Trusted multi-view classification with dynamic evidential fusion. *IEEE Transactions on Pattern Analysis and Machine Intelligence*, 45(2):2551–2566.

Devamanyu Hazarika, Roger Zimmermann, and Soujanya Poria. 2020. Misa: Modality-invariant and-specific representations for multimodal sentiment analysis. In *Proceedings of the 28th ACM international conference on multimedia*, pages 1122–1131.

Douwe Kiela, Suvrat Bhooshan, Hamed Firooz, Ethan Perez, and Davide Testuggine. 2020. Supervised multimodal bitransformers for classifying images and text. *arXiv preprint arXiv:1909.02950*.

Wonjae Kim, Bokyung Son, and Ildoo Kim. 2021. Vilt: Vision-and-language transformer without convolution or region supervision. In *Proceedings of the International Conference on Machine Learning (ICML)*, pages 5583–5594. PMLR.

Simon Kornblith, Mohammad Norouzi, Honglak Lee, and Geoffrey Hinton. 2019. Similarity of neural network representations revisited. In *Proceedings of the International Conference on Machine Learning (ICML)*, pages 3519–3529. PMlR.

Jing Li, Zhibin Wu, and Qiangchang Wang. 2026. Progressive intra- and inter-modality relation learning for multimodal sentiment analysis. *Knowledge-Based Systems*, 334:115088.

Yong Li, Yuanzhi Wang, and Zhen Cui. 2023. Decoupled multimodal distilling for emotion recognition. In *Proceedings of the IEEE/CVF conference on computer vision and pattern recognition*, pages 6631–6640.

Ronghao Lin, Qiaolin He, Ying Zeng, Sijie Mai, Li Huang, and Haifeng Hu. 2026. Affection-guided bottleneck diffusion for missing modality issue in multimodal affective computing. *IEEE Transactions on Affective Computing*, 17(1):708–725.

Fengmao Lv, Xiang Chen, Yanyong Huang, Lixin Duan, and Guosheng Lin. 2021. Progressive modality reinforcement for human multimodal emotion recognition from unaligned multimodal sequences. In *Proceedings of the IEEE/CVF conference on computer vision and pattern recognition*, pages 2554–2562.

Mengmeng Ma, Jian Ren, Long Zhao, Davide Testuggine, and Xi Peng. 2022. Are multimodal transformers robust to missing modality? In *Proceedings of the IEEE/CVF conference on computer vision and pattern recognition (CVPR)*, pages 18177–18186.

Chunlei Meng, Pengbin Feng, Rong Fu, Hoi Leong Lee, Xiaojing Du, Zhaolu Kang, Zeyu Zhang, Weilin Zhou, Chun Ouyang, and Zhongxue Gan. 2026a. Group cognition learning: Making everything better through governed two-stage agents collaboration. *arXiv preprint arXiv:2605.00370*.

Chunlei Meng, Jiabin Luo, Pengbin Feng, Zhenglin Yan, Chengyin Hu, Zhongxue Gan, and Chun Ouyang. 2026b. Mitigating shared-private branch imbalance via dual-branch rebalancing for multimodal sentiment analysis. *arXiv preprint arXiv:2604.25179*.

Chunlei Meng, Jiabin Luo, Zhenglin Yan, Zhenyu Yu, Rong Fu, Zhongxue Gan, and Chun Ouyang. 2026c. Tri-subspaces disentanglement for multimodal sentiment analysis. *arXiv preprint arXiv:2602.19585*.

Chunlei Meng, Ziyang Zhou, Lucas He, Xiaojing Du, Chun Ouyang, and Zhongxue Gan. 2026d. Temporal-spatial decouple before act: Disentangled representation learning for multimodal sentiment analysis. In *ICASSP 2026 - 2026 IEEE International Conference on Acoustics, Speech and Signal Processing (ICASSP)*, pages 11917–11921.

Diego Aarón Moreno-Galván, Roberto López-Santillán, Luis Carlos González-Gurrola, Manuel Montes-Y-Gómez, Fernando Sánchez-Vega, and Adrián Pastor López-Monroy. 2024. Automatic movie genre classification & emotion recognition via a biprojection multimodal transformer. *Information Fusion*, 102:102641.

Teng Niu, Shiai Zhu, Lei Pang, and Abdulmotaleb El Saddik. 2016. Sentiment analysis on multi-view social data. In *International Conference on Multimedia Modeling (MMM)*, pages 15–27.

Wasifur Rahman, Md. Kamrul Hasan, Sangwu Lee, AmirAli Bagher Zadeh, Chengfeng Mao, Louis-Philippe Morency, and Mohammed E. Hoque. 2020. Integrating multimodal information in large pretrained transformers. In *Proceedings of the 58th Annual Meeting of the Association for Computational Linguistics*, pages 2359–2369.

Yao-Hung Hubert Tsai, Shaojie Bai, Paul Pu Liang, J Zico Kolter, Louis-Philippe Morency, and Ruslan Salakhutdinov. 2019. Multimodal transformer for unaligned multimodal language sequences. In *Proceedings of the 57th annual meeting of the association for computational linguistics (ACL)*, pages 6558–6569.

Laurens Van der Maaten and Geoffrey Hinton. 2008. Visualizing data using t-sne. *Journal of machine learning research*, 9(11).

Pan Wang, Qiang Zhou, Yawen Wu, Tianlong Chen, and Jingtong Hu. 2025. Dlf: Disentangled-language-focused multimodal sentiment analysis. In *Proceedings of the AAAI Conference on Artificial Intelligence*, volume 39, pages 21180–21188.

Shicai Wei, Chunbo Luo, and Yang Luo. 2025. Improving multimodal learning via imbalanced learning. In *Proceedings of the IEEE/CVF International Conference on Computer Vision (ICCV)*, pages 2250–2259.

Sheng Wu, Dongxiao He, Xiaobao Wang, Longbiao Wang, and Jianwu Dang. 2025. Enriching multimodal sentiment analysis through textual emotional descriptions of visual-audio content. In *Proceedings of the AAAI Conference on Artificial Intelligence*, volume 39, pages 1601–1609.

Bowen Xu, Xirong Zhang, Xun Wu, and Yating Tian. 2022. Multimodal weighted fusion of transformers for movie genre classification. In *ACM International Conference on Multimedia (MM)*, pages 4530–4538.

Dingkang Yang, Shuai Huang, Haopeng Kuang, Yangtao Du, and Lihua Zhang. 2022. Disentangled representation learning for multimodal emotion recognition. In *Proceedings of the 30th ACM international conference on multimedia*, pages 1642–1651.

Dingkang Yang, Mingcheng Li, Dongling Xiao, Yang Liu, Kun Yang, Zhaoyu Chen, Yuzheng Wang, Peng Zhai, Ke Li, and Lihua Zhang. 2024. Towards multimodal sentiment analysis debiasing via bias purification. In *European Conference on Computer Vision*, pages 464–481. Springer.

Jiuding Yang, Yakun Yu, Di Niu, Weidong Guo, and Yu Xu. 2023a. Confede: Contrastive feature decomposition for multimodal sentiment analysis. In *Proceedings of the 61st Annual Meeting of the Association for Computational Linguistics*, pages 7617–7630.

Yingjie Yang, Hexin Zhang, Kai Han, Tong Wu, Jizhe Song, Jing Liu, and Ziwei Liu. 2023b. Missing modality prediction for unpaired multimodal learning

via joint embedding of unimodal models. In *Proceedings of the IEEE/CVF International Conference on Computer Vision (ICCV)*, pages 1275–1285.

Ziqi Yuan, Wei Li, Hua Xu, and Wenmeng Yu. 2021. Transformer-based feature reconstruction network for robust multimodal sentiment analysis. In *Proceedings of the 29th ACM international conference on multimedia*, pages 4400–4407.

Amir Zadeh, Minghai Chen, Soujanya Poria, Erik Cambria, and Louis-Philippe Morency. 2017. Tensor fusion network for multimodal sentiment analysis. In *Proceedings of the 2017 Conference on Empirical Methods in Natural Language Processing*, pages 1103–1114.

Amir Zadeh, Rowan Zellers, Eli Pincus, and Louis-Philippe Morency. 2016. Multimodal sentiment intensity analysis in videos: Facial gestures and verbal messages. *IEEE Intelligent Systems*, pages 82–88.

AmirAli Bagher Zadeh, Paul Pu Liang, Soujanya Poria, Erik Cambria, and Louis-Philippe Morency. 2018. Multimodal language analysis in the wild: Cmu-mosei dataset and interpretable dynamic fusion graph. In *Proceedings of the 56th Annual Meeting of the Association for Computational Linguistics*, pages 2236–2246.

Hanlei Zhang, Hua Xu, Xin Wang, Qianrui Zhou, Shaojie Zhao, and Jiayan Teng. 2022. Mintrec: A new dataset for multimodal intent recognition. In *Proceedings of the 30th ACM International Conference on Multimedia*, page 1688–1697.

Qingyang Zhang, Haitao Wu, Changqing Zhang, Qinghua Hu, Huazhu Fu, Joey Tianyi Zhou, and Xi Peng. 2023. Provable dynamic fusion for low-quality multimodal data. In *Proceedings of the 40th International Conference on Machine Learning (ICML)*.

Xiaohui Zhang, Jaehong Yoon, Mohit Bansal, and Huaxiu Yao. 2024. Multimodal representation learning by alternating unimodal adaptation. In *Proceedings of the IEEE/CVF Conference on Computer Vision and Pattern Recognition (CVPR)*.

Aoqiang Zhu, Min Hu, Xiaohua Wang, Jiaoyun Yang, Yiming Tang, and Ning An. 2025. Proxy-driven robust multimodal sentiment analysis with incomplete data. In *Proceedings of the 63rd Annual Meeting of the Association for Computational Linguistics (Volume 1: Long Papers)*, pages 22123–22138.

A Related Works

A.1 Multimodal Learning

Multimodal learning has been widely studied in tasks such as sentiment analysis, intent recognition, and vision language understanding. Early works such as TFN (Zadeh et al., 2017), MMBT (Kiela et al., 2020), and ViLT (Kim et al., 2021) encode each modality separately and project the resulting features into a shared latent space, where a joint representation is learned for prediction. For video and audio–text modeling, MAG-BERT (Rahman et al., 2020), MulT (Tsai et al., 2019), and other transformer-based models use cross-modal attention to capture temporal interactions between language, vision, and audio. Methods such as MISA (Hazarika et al., 2020), MCIS (Yang et al., 2024), CGGM (Guo et al., 2024), and DMD (Li et al., 2023) explicitly model modality-invariant and modality-specific factors to obtain more structured multimodal representations for sentiment analysis. Most existing methods fuse all modalities in a single latent space, which biases representations toward shared factors and tends to wash out modality-private cues, especially under noisy or partially missing inputs. Despite their differences in architecture and training strategies, most of these methods ultimately concentrate both supervision and fusion in a single latent space. Strong cross-modal alignment or joint optimization tends to emphasize features that are predictive across modalities and for the target label, while subtle modality-private cues with weak cross-modal correlation are downweighted or compressed. As a result, the joint representation is often biased toward shared factors, and modality-specific information is easily diluted, especially under noisy or partially missing modalities.

A.2 Multimodal Fusion Mechanism

Many works design more flexible fusion mechanisms to handle modality heterogeneity. Simple concatenation and late fusion baselines (Gao et al., 2024) combine unimodal features at the feature or decision level, but ignore fine-grained cross-modal interactions. FDMER (Yang et al., 2022) employs dynamic fusion with mutual enhancement and regularization, while MCIS (Yang et al., 2024) and CGGM (Guo et al., 2024) incorporate contrastive or graph-based modules to refine multimodal representations. EAU (Gao et al., 2024) explicitly models aleatoric uncertainty with stable unimodal augmentation and robust multimodal integration to obtain compact and noise-resistant joint representations. EMOE (Fang et al., 2025) integrates emotion-guided subspace interactions, DLF (Wang et al., 2025) adopts dual-level fusion blocks, and DEVA (Wu et al., 2025) uses decoupled visual–acoustic streams with attentive fusion to enhance emotion recognition robustness. However, existing fusion mechanisms still fuse all modalities in a single joint embedding, which tends to suppress modality private cues.

B Methodological Details and Theoretical Rationale

This appendix provides the details omitted from the main methodology because of space constraints. The main paper defines the AHRA architecture and the training objective; here we clarify the CKA diagnostic, the shared–private motivation, and the exact interpretation of the correlation and gate regularizers.

B.1 CKA Diagnostic for Semantic Granularity Mismatch

For each modality m and semantic level ℓ, we compute sample-level features $\mathbf{h}_{\ell,i}^{(m)} = \mathrm{Pool}(H_{\ell,i}^{(m)})$ for all validation samples. Let $X_\ell^{(m)} \in \mathbb{R}^{n\times d}$ stack these vectors. We use a centered linear representation kernel

$$K_\ell^{(m)} = \Gamma X_\ell^{(m)} (X_\ell^{(m)})^\top \Gamma, \qquad \Gamma = I_n - \frac{1}{n}\mathbf{1}\mathbf{1}^\top. \tag{23}$$

For single-label classification, the label matrix $Y \in \mathbb{R}^{n\times C}$ is one-hot. For multi-label classification such as MM-IMDB, Y is multi-hot. In both cases, the label kernel is

$$K_y = \Gamma Y Y^\top \Gamma. \tag{24}$$

For regression datasets such as CMU-MOSI and CMU-MOSEI, we use the scalar label vector $y \in \mathbb{R}^n$ and set

$$K_y = \Gamma y y^\top \Gamma. \tag{25}$$

The empirical CKA score is

$$\mathrm{CKA}\big(K_\ell^{(m)}, K_y\big) = \frac{\langle K_\ell^{(m)}, K_y\rangle_F}{\|K_\ell^{(m)}\|_F \|K_y\|_F}. \tag{26}$$

This score is used only to diagnose the layer at which each modality becomes most label-informative. It is not optimized during AHRA training and should not be read as a proof of semantic

granularity mismatch. The diagnostic supports the architectural choice of retaining multiple semantic levels when different modalities peak at different depths.

B.2 Why Flat Alignment Can Suppress Private Factors

We give a simple latent-factor argument for why single-space cross-modal alignment can attenuate modality-private cues. Consider two modalities m and m' at one semantic level, with zero-mean representations

$$h^{(m)} = A^{(m)}c + B^{(m)}u^{(m)} + \epsilon^{(m)}, \tag{27}$$

$$h^{(m')} = A^{(m')}c + B^{(m')}u^{(m')} + \epsilon^{(m')}, \tag{28}$$

where c is a shared latent factor, $u^{(m)}$ and $u^{(m')}$ are modality-private factors, and the noise terms are zero mean. Assume the shared, private, and noise factors are mutually uncorrelated across the groups. A flat alignment objective with linear projections W_m and $W_{m'}$ is

$$\mathcal{J} = \mathbb{E}\left\|W_m h^{(m)} - W_{m'} h^{(m')}\right\|_2^2. \tag{29}$$

Expanding Eq. (29) under the uncorrelated-factor assumption gives

$$\begin{aligned}\mathcal{J} = &\left\|W_m A^{(m)} - W_{m'} A^{(m')}\right\|_{\Sigma_c}^2 \\ &+ \left\|W_m B^{(m)}\right\|_{\Sigma_{u_m}}^2 + \left\|W_{m'} B^{(m')}\right\|_{\Sigma_{u_{m'}}}^2 \\ &+ \|W_m\|_{\Sigma_{\epsilon_m}}^2 + \|W_{m'}\|_{\Sigma_{\epsilon_{m'}}}^2 ,\end{aligned} \tag{30}$$

where $\|Q\|_\Sigma^2 = \mathrm{tr}(Q\Sigma Q^\top)$. The shared component is rewarded when $W_m A^{(m)}$ and $W_{m'} A^{(m')}$ match. By contrast, the private components appear only as positive penalty terms because $u^{(m)}$ and $u^{(m')}$ are not predictable across modalities. Therefore, if the model relies only on flat alignment and lacks a private path, minimizing alignment pressure can shrink the private directions $W_m B^{(m)}$ and $W_{m'} B^{(m')}$. AHRA addresses this by keeping private streams and routing them through modality-specific experts rather than forcing all evidence into a single aligned space.

B.3 Interpretation of the Decoupling Losses

The shared alignment loss in the main paper uses dimension-wise batch standardization followed by a cross-correlation target. This should be distinguished from full whitening. Dimension-wise standardization ensures approximately zero mean and unit variance for each coordinate in a mini-batch, but it does not remove all within-modality covariance. Full whitening would require multiplying by an inverse covariance square root.

The finite-batch identity target should be interpreted as a regularizer rather than an exactly attainable constraint. Let $Z_m, Z_{m'} \in \mathbb{R}^{B\times d_{\mathrm{sh}}}$ be the standardized shared representations in a mini-batch. The empirical matrix $C = Z_m^\top Z_{m'}/B$ satisfies

$$\mathrm{rank}(C) \le \min(\mathrm{rank}(Z_m), \mathrm{rank}(Z_{m'})) \le B. \tag{31}$$

With centered standardized features, the effective rank is at most $B-1$ in the usual case. Therefore, when $d_{\mathrm{sh}} > B$, as in our default setting $d_{\mathrm{sh}} = 256$ and $B = 32$, C cannot equal the full-rank identity matrix $I_{d_{\mathrm{sh}}}$ in a single mini-batch. The identity-shaped target is used as a stochastic correlation-shaping surrogate that encourages coordinate agreement and redundancy reduction over training.

The private loss penalizes linear cross-correlation between streams. Zero covariance is equivalent to independence only under additional assumptions such as joint Gaussianity. For general neural representations, $\mathcal{L}_{\mathrm{pr}}$ should be interpreted as encouraging linear decorrelation and reducing duplicated linear factors, not as a guarantee of full disentanglement.

B.4 Interpretation of the Foreground Exam

The foreground exam produces sample-wise soft gates $\beta_{\ell,i,t}^{(m)}$ over private tokens. The rate term in $\mathcal{L}_{\mathrm{exam}}$ controls the expected number of private tokens passed to the private expert, while the confidence term penalizes uncertain values near 0.5. These terms alone do not prove that selected tokens are semantically foreground or task-relevant. Task relevance is learned through gradients from $\mathcal{L}_{\mathrm{task}}$ and the subsequent expert/fusion modules, while $\mathcal{L}_{\mathrm{exam}}$ controls sparsity and stability.

The shared stream used in the private expert is interpreted as contextual conditioning. In the main text this is written as $E_{\mathrm{pr},\ell}^{(m)}(R_{\ell,\mathrm{FG}}^{(m)}; c_\ell^{(m)})$, where $c_\ell^{(m)} = \mathrm{Ctx}(S_\ell^{(m)})$. This notation does not introduce a new training objective; it clarifies that private-token enhancement is anchored in $R_{\ell,\mathrm{FG}}^{(m)}$ while being calibrated by same-level shared context.

B.5 Interpretation of the Hierarchical Regularizer

The main paper keeps the original inter-level regularizer

$$\mathcal{L}_{\text{hier}} = \lambda_{\text{hier}} \sum_{\ell=1}^{L} \rho_\ell \log(\rho_\ell + \varepsilon). \tag{32}$$

Ignoring the numerical constant ε, this is $-\lambda_{\text{hier}} H(\rho)$, where $H(\rho)$ is the entropy of the inter-level distribution. Since the training objective is minimized and $\lambda_{\text{hier}} > 0$, this term encourages higher entropy, i.e., more distributed level usage. It should therefore be described as a level-diversity or anti-collapse stabilizer, not as a concentration or sparsity penalty. The inter-level gate can still produce non-uniform level weights because the task loss and the gate network remain sample-dependent.

B.6 Training Procedure

For each mini-batch, AHRA is optimized as follows.

1. Extract multi-level unimodal features $\{H_\ell^{(m)}\}_{\ell=1}^{L}$ for all available modalities $m \in \mathcal{M}$.
2. Project each level into shared and private streams using Eq. (5).
3. Compute $\mathcal{L}_{\text{sh}}$ and $\mathcal{L}_{\text{pr}}$ from mini-batch cross-correlations.
4. Apply AEA: route shared streams through $E_{\text{sh},\ell}$ and foreground-weighted private streams through $E_{\text{pr},\ell}^{(m)}$.
5. Apply HMEC: compute intra-level expert weights $\alpha_{e,\ell}$, level descriptors $\bar{z}_\ell$, inter-level weights ρ_ℓ, and z_{final}.
6. Compute $\mathcal{L}_{\text{task}}$, $\mathcal{L}_{\text{exam}}$, $\mathcal{L}_{\text{col}}$, and $\mathcal{L}_{\text{hier}}$.
7. Update all trainable parameters by minimizing $\mathcal{L}_{\text{total}}$ with AdamW.

C Dataset Details

We evaluate AHRA on six multimodal benchmarks, including four classification datasets and two trimodal sentiment analysis datasets.

Classification datasets. The first group contains MM-IMDB (Ma et al., 2022), Food101 (Bossard et al., 2014), MVSA-Single (Niu et al., 2016), and MIntRec (Zhang et al., 2022). MM-IMDB consists of 25,959 movie samples, where each sample contains a movie poster and a synopsis for multi-label genre prediction. Food101 provides over 100,000 image-text pairs from 101 food categories for fine-grained food classification. MVSA-Single contains 4,869 social media image–text pairs annotated with three-way sentiment labels. MIntRec includes 2,224 trimodal samples from 20 intent categories. Following EAU (Gao et al., 2024), we report accuracy, micro-F1, and macro-F1 on these four datasets.

Sentiment analysis datasets. The second group contains CMU-MOSI (Zadeh et al., 2016) and CMU-MOSEI (Zadeh et al., 2018). CMU-MOSI includes 2,199 monologue video clips, while CMU-MOSEI contains 22,856 video clips. Both datasets provide aligned language, acoustic, and visual features, together with sentiment scores in $[-3, 3]$, ranging from strongly negative to strongly positive. Following EMOE (Fang et al., 2025), we report MAE, Acc-7, and F1 on these two datasets.

Table 9: Hyperparameter settings used in our experiments.

Hyperparameter	Value
Hierarchy levels L	3
Internal dimensions $(d_{\text{sh}}, d_{\text{pr}})$	$(256, 256)$
Foreground target ratio $\pi_{m,\ell}$	0.30
Temperatures $(\tau_{\text{intra}}, \tau_{\text{inter}})$	$(1.0, 1.0)$
Decoupling weights $(\lambda_{\text{sh}}, \lambda_{\text{pr}})$	$(0.1, 0.1)$
Exam weights $(\lambda_{\text{rate}}, \lambda_{\text{conf}})$	$(1.0, 0.1)$
Gate regularizers $(\lambda_{\text{fair}}, \lambda_{\text{hier}})$	$(0.1, 0.1)$
Gate priors $(\eta_{\text{L}}, \eta_{\text{V}}, \eta_{\text{A}})$	$(0.1, 0.1, 0.1)$
Optimizer	AdamW
Learning rate	1×10^{-5}
Batch size	32
Max epochs	35

D Implementation Hyperparameters

To ensure reproducibility, we summarize the main hyperparameter settings used in our experiments in Table 9. Unless otherwise specified, the same configuration is adopted across all datasets.

E Model Zoo

We compare AHRA with image-text classification baselines ConCat, LateFu, GMU, MGMU, MMBT, TMC, QMF, EAU, MLA, BPMulT, and ARL (Gao

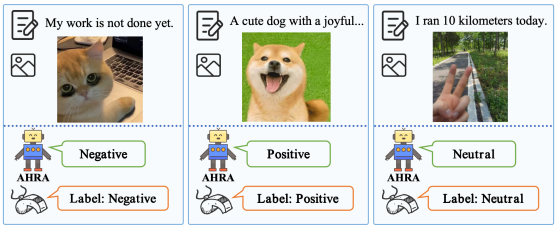

Figure 5: Qualitative multimodal recognition results of AHRA in a real-world sentiment analysis case.

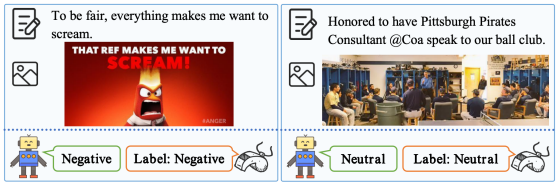

Figure 6: Qualitative multimodal recognition results of AHRA on the sentiment analysis task.

et al., 2024; Arevalo et al., 2017; Xu et al., 2022; Kiela et al., 2020; Han et al., 2023; Zhang et al., 2023, 2024; Moreno-Galván et al., 2024; Wei et al., 2025), multimodal intent baselines MAG-BERT, MulT, MISA, DLF, TSDA, and EMOE (Rahman et al., 2020; Tsai et al., 2019; Hazarika et al., 2020; Wang et al., 2025; Meng et al., 2026d; Fang et al., 2025), trimodal sentiment baselines TFN, PMR, FDMER, DMD, MCIS, CGGM, ConFEDE, DiCMoR, DEVA, and I2RL (Zadeh et al., 2017; Lv et al., 2021; Yang et al., 2022; Li et al., 2023; Yang et al., 2024; Guo et al., 2024; Yang et al., 2023a; Gao et al., 2024; Wu et al., 2025; Li et al., 2026), and robustness baselines following PEFT (Yang et al., 2023b). The tables therefore use compact method names without repeated citations.

F Statistical Reliability of AHRA

All experiments were repeated five times with different random seeds. As shown in Table 10, we report mean and standard deviation for AHRA on all benchmarks, together with variance and 95% confidence intervals to assess statistical stability. The statistical evidence confirms that AHRA exhibits high stability across modalities, dataset scales, and tasks, with consistently small variance and narrow confidence intervals. Combined with the ablation studies and robustness experiments, these results validate that the performance improvements of AHRA arise from principled architectural design rather than randomness.

Table 10: Statistical results of AHRA across all benchmarks. Mean and standard deviation are computed over 5 runs with different random seeds.

Dataset	Metric	Mean $\pm$ Std	Var.	95% CI
Image-text and Multimodal Classification (%)				
MM -IMDB	F1-mic	69.18 ± 0.33	0.11	[68.76, 69.60]
	F1-mac	63.24 ± 0.41	0.17	[62.66, 63.82]
Food101	Acc	95.06 ± 0.18	0.03	[94.78, 95.34]
	F1	94.21 ± 0.21	0.04	[93.88, 94.54]
MVSA -Single	Acc	79.84 ± 0.26	0.07	[79.44, 80.24]
	F1	78.59 ± 0.31	0.10	[78.13, 79.05]
Multimodal Intent Recognition (MIntRec, %)				
MIntRec	Acc	73.02 ± 0.27	0.07	[72.68, 73.36]
	F1	72.16 ± 0.30	0.09	[71.79, 72.53]
	Precision	72.97 ± 0.34	0.12	[72.55, 73.39]
	Recall	71.36 ± 0.29	0.08	[70.96, 71.76]
Trimodal Sentiment Analysis (MOSI / MOSEI)				
CMU -MOSI	MAE	0.702 ± 0.006	3.6×10^{-5}	[0.695, 0.709]
	Acc-7	48.77 ± 0.37	0.14	[48.28, 49.26]
	F1	86.36 ± 0.28	0.08	[85.96, 86.76]
CMU -MOSEI	MAE	0.522 ± 0.004	1.6×10^{-5}	[0.517, 0.527]
	Acc-7	55.65 ± 0.25	0.06	[55.30, 56.00]
	F1	86.66 ± 0.19	0.04	[86.39, 86.93]

G Additional Qualitative Results

Versatility Across Semantic Domains. We further provide qualitative examples to examine the generalization capability of AHRA across different multimodal tasks, including sentiment analysis and movie genre recognition. As shown in Fig. 5 and Fig. 6, AHRA can capture nuanced affective cues from complex real-world image-text scenarios, leading to reliable sentiment predictions. In addition, the results on the IMDb dataset in Fig. 7 show that AHRA can also support high-level semantic reasoning for multi-label movie genre prediction. These observations suggest that the adaptive expert

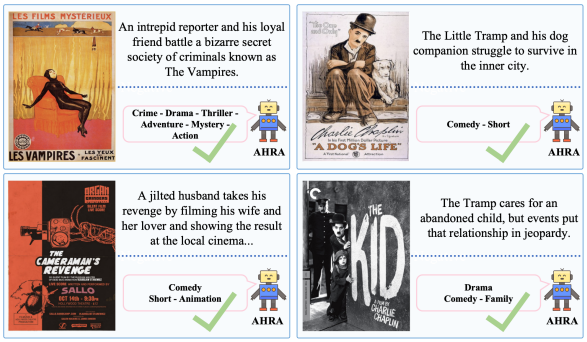

Figure 7: Qualitative multimodal recognition results of AHRA on the movie category recognition task.

collaboration and hierarchical fusion design enable AHRA to align and integrate heterogeneous multimodal evidence across diverse semantic domains.

H Representation Visualization

To further examine the representation geometry learned by AHRA, we apply t-SNE (Van der Maaten and Hinton, 2008) to project the final multimodal embeddings on MVSA-Single into a two-dimensional space. As shown in Fig. 8, the full AHRA forms the most compact and class-separable sentiment clusters, indicating that the joint use of shared–private factorization, adaptive expert routing, and hierarchical co-fusion produces discriminative multimodal representations.

The ablated variants reveal how different designs contribute to this geometry. Removing HMEC leads to more diffuse decision regions and heavier boundary overlap, suggesting that intra-level expert coordination and inter-level semantic selection are important for organizing evidence across semantic levels. Removing AEA further weakens cluster compactness, which indicates that adaptive private-token enhancement helps preserve task-relevant modality-specific cues before final fusion. The variant without $\mathcal{L}_{\text{dec}}$ exhibits the most severe class mixing, showing that shared alignment and private decorrelation are crucial for maintaining a structured shared–private representation space. These visual patterns are consistent with the quantitative ablation results and provide qualitative evidence that AHRA mitigates modality-private cue dilution while improving the discriminability of final multimodal embeddings.

I Sensitivity to Regularization Hyperparameters

We evaluate the sensitivity of AHRA to the main regularization hyperparameters that control shared–private decoupling, the foreground exam, and hierarchical gating. Instead of sweeping all coefficients on all datasets, we probe each group of terms on benchmarks where their effects are most directly reflected in the evaluation metrics.

We first study the decoupling loss $\mathcal{L}_{\text{dec}}$ in Eq. (11) and the exam loss $\mathcal{L}_{\text{exam}}$ in Eq. (16) on CMU-MOSI (Zadeh et al., 2016) and CMU-MOSEI (Zadeh et al., 2018). These terms act on the representation level: λ_{sh} and λ_{pr} shape the alignment and separation of shared and private subspaces, while λ_{rate} and λ_{conf} control how strongly the foreground budget and gate confidence are enforced. Fine-grained sentiment regression on MOSI/MOSEI is particularly sensitive to such changes in token-level structure and modality-private cues. As shown in Fig. 9, we therefore vary each of $\lambda_{\text{sh}}, \lambda_{\text{pr}}, \lambda_{\text{rate}}, \lambda_{\text{conf}}$ around the default setting, keeping the others fixed, and monitor MAE and Acc-7. Across a broad range of values, both datasets exhibit only mild fluctuations; performance degrades noticeably only when decoupling is almost removed or when the exam regularization becomes either too weak or too strong. This pattern is consistent with the design goal of AHRA: as long as a structured shared–private decomposition is preserved and a moderate fraction of private tokens is selected, the model maintains stable sentiment performance without aggressive tuning.

We then analyze the gating regularizers $\mathcal{L}_{\text{col}}$ and $\mathcal{L}_{\text{hier}}$ on Food101 (Bossard et al., 2014) and MIntRec (Zhang et al., 2022). These terms mainly stabilize private-expert usage and inter-level routing, rather than directly modifying token representations. Specifically, $\mathcal{L}_{\text{col}}$ discourages systematic under-use of modality-specific experts, while $\mathcal{L}_{\text{hier}}$ controls the strength of the level-diversity stabilizer. As shown in Fig. 10, accuracy and F1 remain stable around the default setting, with degradation only at extreme values. Very small λ_{fair} can under-use private experts, whereas very large λ_{fair} forces nearly uniform expert usage and weakens adaptive routing. Similarly, removing or weakening $\mathcal{L}_{\text{hier}}$ can make inter-level routing less stable, while an overly large λ_{hier} makes level usage too diffuse and reduces the gate's ability to emphasize the most informative semantic scale for a given sample.

Overall, these studies indicate that AHRA is robust to the precise choice of regularization hyperparameters. The decoupling and exam coefficients can be tuned within a broad range without destabilizing fine-grained sentiment regression, and the gating regularizers admit similarly wide margins on diverse classification benchmarks. This robustness simplifies deployment in new multimodal settings, since reasonable default values already yield strong performance without extensive hyperparameter search.

J Efficiency Analysis

Table 11 reports the computational efficiency of AHRA on CMU-MOSI in terms of parameter count, average training time per epoch, and pre-

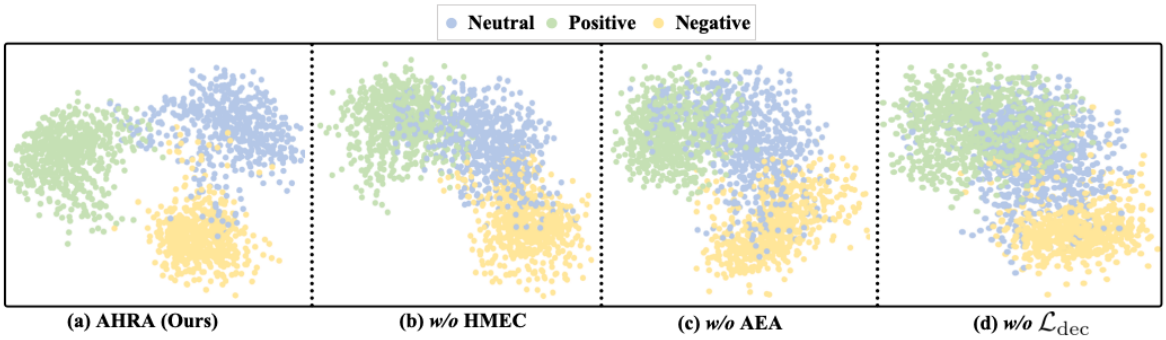

Figure 8: t-SNE visualization of final multimodal embeddings on MVSA-Single under key AHRA designs. The full AHRA yields the most compact intra-class structures and the clearest inter-class separation. Removing HMEC weakens semantic-level aggregation, removing AEA reduces adaptive private-token enhancement, and removing $\mathcal{L}_{\text{dec}}$ causes the strongest class overlap due to weakened shared–private structuring.

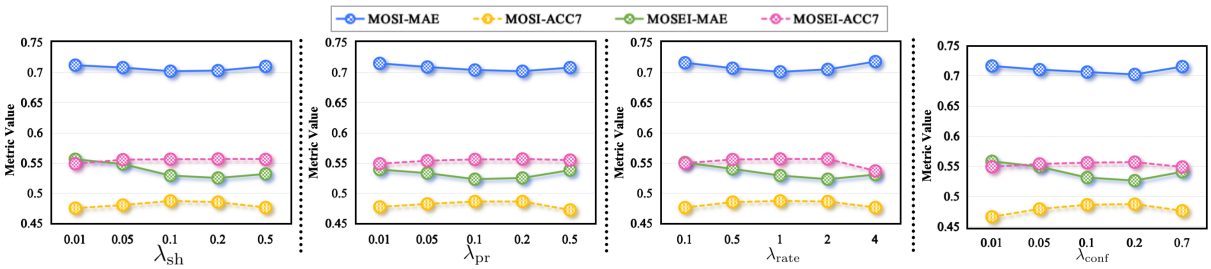

Figure 9: Sensitivity of AHRA to the decoupling loss $\mathcal{L}_{\text{dec}}$ and exam regularization $\mathcal{L}_{\text{exam}}$ on CMU-MOSI and CMU-MOSEI.

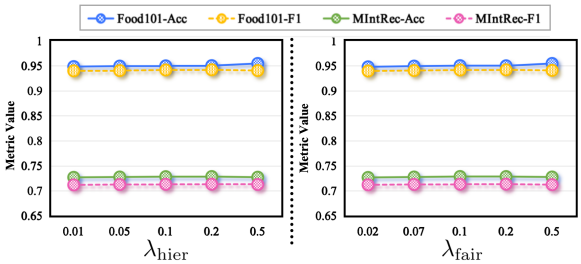

Figure 10: Sensitivity of AHRA to the gating regularizers $\mathcal{L}_{\text{col}}$ and $\mathcal{L}_{\text{hier}}$ on the image–text and multimodal classification benchmarks Food101 (Bossard et al., 2014) and MIntRec (Zhang et al., 2022).

dictive performance. AHRA contains 122.78M parameters, which is comparable to TFR-Net and DMD, slightly larger than PRMF, and substantially smaller than ConFEDE. Although AHRA introduces multi-level shared–private factorization, adaptive expert routing, a foreground exam, and hierarchical co-fusion, its training time remains moderate at 26.75s per epoch. It is slower than highly simplified or reconstruction-light baselines such as TFR-Net and PRMF, but is clearly more efficient than heavier multi-module or generative-style frameworks such as DMD, ConFEDE.

This efficiency mainly comes from the design of AHRA. First, AHRA operates in the representation space rather than reconstructing high-dimensional modalities, avoiding expensive generative decoding. Second, the shared–private factorization is implemented with lightweight linear projections, while AEA restricts cross-modal reasoning to the shared subspace and applies modality-specific experts only to foreground-weighted private streams. Third, HMEC decomposes fusion into intra-level expert coordination and inter-level semantic aggregation, replacing dense all-to-all fusion with compact sample-adaptive gating. As a result, AHRA introduces structured hierarchical reasoning without excessive computational overhead.

More importantly, the additional cost is accompanied by consistent performance gains. Compared with the competitive baselines in Table 11, AHRA achieves the best MAE and Acc-7 on CMU-MOSI, while maintaining the strongest F1 among the compared methods. These results indicate that AHRA does not pursue efficiency by simplifying multimodal interaction; instead, it achieves a favorable accuracy–efficiency trade-off by allocating computation to the most informative private tokens,

Table 11: Computational efficiency analysis on CMU-MOSI. We report total parameter counts and average training time per epoch measured under the same experimental environment, together with the corresponding predictive performance.

Model	Params(M)	Time/Epoch(S)	MAE(↓)	Acc-7(%)	F1(%)
TFR-Net (Yuan et al., 2021)	124.33	11.53	0.805	40.82	83.57
ConFEDE (Yang et al., 2023a)	246.98	40.12	-	42.33	85.53
DMD (Li et al., 2023)	122.06	35.97	0.744	43.88	83.55
PRMF (Zhu et al., 2025)	117.26	18.62	0.726	44.31	82.69
ABDiff (Lin et al., 2026)	132.12	140.20	0.715	45.16	86.54
AHRA (Ours)	**122.78**	**26.75**	**0.702±0.006**	**48.77±0.37**	**86.36±0.28**

experts, and semantic levels.